Metallophosphazene Precursor Routes to Solid-State Deposition of Metallic and Dielectric Micro- and Nanostructures on Si and SiO_2

Carlos Díaz,[a*] Maria Luisa Valenzuela,[b] Antonio Laguna,[c] Vladimir Lavayen,[d] Josefina Jiménez,[c] Lynn A. Power,[e] and Colm O'Dwyer [e*]

[a] *Departamento de Química, Facultad de Ciencias, Universidad de Chile, Las Palmeras 3425, Santiago, Chile*

[b] *Departamento de Ciencias Quimica, Facultad de Ecologia y Recursos Naturales Universidad Andres Bello, Av. Republica 275, Santiago, Chile*

[c] *Departamento de Química Inorgánica, Instituto de Ciencia de Materiales de Aragón, Universidad de Zaragoza-C.S.I.C., 50009, Zaragoza, Spain*

[d] *Departamento de Física, Universidad Técnica Federico Santa María, Valparaíso 2390123 Chile*

[e] *Department of Physics, and Materials & Surface Science Institute, University of Limerick, Limerick, Ireland*

[*] Corresponding author: E-mail: cdiaz@uchile.cl; Tel: +56 2 9787367; Fax: +56 2 271388; E-mail: colm.odwyer@ul.ie; Tel: +353 61 202288

Abstract

We present a method for the preparation and deposition of metallic micro- and nanostructures deposited on silicon and silica surfaces by pyrolysis in air at 800°C of the corresponding metallophosphazene (cyclic or polymer). Atomic force microscopy studies reveal that the morphology is dependent on the polymeric or oligomeric nature of the phosphazene precursor, on the preparation method used as well as on the silicon substrate surface (crystalline or amorphous) and its prior inductively couple plasma etch treatment.

Micro- and nanoscale structures and high surface area thin films of gold, palladium, silver and tin were successfully deposited from their respective newly synthesized precursors. The characteristic morphology of the deposited nanostructures resulted in varied roughness and increase in surface area, observed to be dependent on the precursor and the metal center. In contrast to island formation from noble metal precursors, we also report a coral of SnP_2O_7 growth on Si and SiO_2 surface from the respective Sn polymer precursor, leaving a self-affine fractal structure with a well-defined roughness exponent which appears to be independent (within the experimental error) of the average size of islands. The nature of the precursor will be shown to influence the degree of surface features and the mechanism of their formation is presented. The method reported here constitutes a new route to the deposition of single-crystal metallic, oxidic and phosphate nanostructures and thin films on technologically relevant substrates.

Introduction

Due to their low resistivity and good corrosion resistance, noble metal, transition metal and silicon thin films have a variety of applications as contacts and conductors in micro- and burgeoning nanoelectronics research and eventual development[1-3]. The fabrication of metallic micro- and nanostructures on dielectric or semiconductor surfaces is a key technology in nanoelectronic engineering. Two principal methods are generally used to prepare metallic thin films: vapor-phase deposition and liquid-based growth, but few thin film methods utilizing precursors in their solid-state have been reported[4]. To realize inorganic nanostructured materials,[5] tedious and sometimes expensive methods such as dip-pen nanolitography,[6,7] nanosphere lithography[8] or ion/electron beam lithography[9] have been primarily used. For gold and other noble metals, several chemical deposition methods have been reported,[2,9-11] in addition to related electrodeposition techniques[12]. A more sophisticated method using a nanofountain probe to directly deposit gold particles has been recently described,[13] owing to the need for new strategies for particle and structure deposition, including catalyst particles for seeding nanowire growth[14]. The formation of structures with either well-defined or new electrical or optical properties will always be influenced by whether they are formed top-down or bottom-up. The This organometallic and metallic pyrolytic approach to metal structure deposition is inherently bottom up; for certain properties/applications, this is often superior to top-down approaches where feature placement and/or lithography is not a necessity.

In addition to controlled deposition, gold, silver and other noble metal nanostructures and nanostructured thin films are important in surface-enhanced Raman scattering (SERS), surface-enhanced infrared absorption (SEIRA), localized surface plasmon polariton-based sensors and surface plasmon-mediated nanostructures for biomolecule detection in the optical near field[15]. While the fabrication of porous gold, silver and copper (and many other metals) is relatively straightforward, the realization of SERS/SEIRA deposits on surfaces of other valve and transition metals via designed

organometallic routes offers potentially much more flexibility in phase control of the deposited metals, and also in controlled roughness generation and the formation of fractally rough surfaces[16]. This control allows the potential formation of multicatalytic surfaces using Pt and V-containing organometallic and metallic derivatives of phosphazenes and related macromolecules, for example.

Surprisingly few methods to deposit nanostructured metallic oxides on surfaces via solid-state chemical routes have been reported.[17] Since the formation of individual metal and metal-oxide nanostructures and nanostructured films is now possible via this process, metal-pyrophosphates are also formed during pyrolysis.[18] This is advantageous as metal-pyrophosphates are noted as good proton conductors in intermediate temperature fuel cells and new methods of surface coverage with these compounds are currently being sought[19]. The route that is described here also affords a simple method to positive and negative thermal expansion materials as individual nanostructures or as a deposited film. Pyrophosphates $A^{IV} M_2{}^{V}O_7$, where the A^{IV} cation includes Zr, Ti, Mo, Re, W, Th, U, Pu, Ce, Hf, Pb, Sn, Ge, and Si; M^{V} = P, V, or As, are known for their unusual high temperature behaviour.[20] Thermal expansion is a necessary consideration in a number of applications where increases and decreases in temperatures can affect physical dimensions, stability, integrity, and mechanical properties of materials; predictably roughened surfaces are also beneficial in maximizing cooling.

Here we present an alternative and simple solid-state process to form noble metal and pyrophosphate micro- and nanostructures on Si and SiO_2 surfaces by pyrolysis of cyclic or polymeric metallophosphazenes, requiring neither expensive clean-room nor vacuum equipment to achieve uniphasic and pure deposition, summarized in Scheme 1. Considering the interest in the determinate and controlled assembly of nanoparticles and nanostructures on surfaces, we present a new method of micro- and nanoscale metal, metal oxide and metal pyrophosphate deposition on surfaces. We also report the formation of self-affine fractal transition metal-containing surface films comprising a coral nanostructured SnP_2O_7 layer.

The phosphazenes used in this work as precursors of micro- and nanostructures on Si and SiO_2 surfaces are shown in Scheme 2.

Experimental Section

Synthesis of phosphazenes used as precursors

The derivatives containing gold, silver or tin (1, 2, 4, 5 and 6) were prepared according to published procedures.[21] Polyphosphazene 3 was synthesized using a similar method to that described for 1 and 2 (see Supporting Information).

Preparation and Deposition of the Au, Ag, Pd and Sn Structures

Method A

A drop of CH_2Cl_2 solution containing polymer (1) was drained over either a silicon or oxidized silicon surface and the solvent evaporated. The concentration of the precursor suspension was always in the range 10^{-3} - 10^{-2} g mL^{-1}. The Si or SiO_2 wafer (with 400 nm of thermally grown oxide) was subsequently pyrolyzed at 800°C using a predefined temperature program where the polymer samples were heated at a rate of 10°C min^{-1} from room temperature to 800°C under a constant air flow of 120 mL min^{-1}. The resulting depositions give uniform areal coverage for each precursor.

Method B

The solid polymer was dusted on the silicon or oxidized silicon wafer polymer/oligomer and pressed with a flat polished metallic surface. The pre-pyrolytic pressing ensured the best coverage of the solid precursor and minimized locally thicker deposits from the dusting procedure, and then pyrolyzed at 800°C using the previously described temperature program, also under air.

Substrate etching and cleaning

The (100) silicon wafer was etched with the commercial products SF_6 and C_4H_8 in an inductively coupled plasma reactor, to a typical etch depth of 50-200 nm. It was subsequently cleaned by the standard RCA process and hydrophilized in water[22].

Analysis of the metallic nanostructured deposits

The morphological structure of the metallic structures on silicon and oxidized silicon surfaces using both methods A and B were examined by atomic force microscopy (AFM) using a Veeco Enviroscope in contact mode. To analyze the pattern formation, the self-correlated AFM image was processed by the WSxM program. Topological information was supplemented by lateral force and phase modulation imaging, respectively, to determine adhesion force changes and composition differences in the surfaces examined. Soft Si_3N_4-tipped cantilevers with a spring constant of 0.12 nN nm^{-1} were used in contact mode. X-ray diffraction measurements were conducted on a Siemens D-5000 diffractometer with θ-2θ geometry using Cu-Kα radiation (40 kV, 30 mA). Energy dispersive X-ray analysis was carried out using a Hitachi SU-70 field emission scanning electron microscope operating at 10 kV equipped with an Oxford Instruments X-max 50 mm^2 solid-state EDX detector.

Results and Discussion

Structure deposition from pyrolysis of the respective metallophosphazene

Both Methods A and B (see Experimental section) were used to deposit the nanostructured products on Si as well as SiO_2 surfaces, and also on ICP etched Si surfaces. Scheme 3 shows a schematic illustration of these methods. Since precursors were synthesized for Au, Ag, Pd and Sn, we first describe the surface morphology and mechanism of deposition of noble metal, metal oxide and pyrophosphate micro and nanostructures as individual islands and thin films. Figure 1 shows a series of

AFM images of the as-deposited structures after pyrolysis of the metallophosphazene derivative directly on the surface, using Method A. On both Si and SiO_2 surfaces, the product from the Au (Figs 1a,e) containing precursor (1) always forms islands with sizes in the range 200 nm – 2 μm and average heights of 80 nm – 1.6 μm respectively. For the more reactive Ag, pyrolysis of its precursor (2) results in quasi-film formation on Si, where the deposit is characterized by a surface coverage interspersed with characteristic craters with an average diameter of 1.3 μm. Each of these features is located within a grain-like domain of Ag deposit. In contrast to the Au, the Ag deposit under identical conditions on thermally grown SiO_2 in Fig. 1f, is markedly different. The surface morphology is characterized a rough deposit of striated Ag structures interspersed by large hillocks of Ag metal. A shaded AFM image highlighting these features is shown in Supporting Information, Fig. S1. The feature sizes of Ag on SiO_2 by this method are similar to that of Au under similar conditions, *i.e.* islands of ~1 μm in height and ~3 μm in diameter are found. In general, the tendency for Ag-containing precursors such as (2) is to form films. On Si the film is incomplete whereas on SiO_2 the deposition coats the entire surface but also forms locally higher features in the form of hillocks. For the Pd pyrolytic product from (3), we observe uniformly dispersed and definite tear-drop islands of metal Pd on Si (see Fig. 1c and inset image), and in contrast a very rough thick film deposit of pure Pd on SiO_2, shown in Fig. 1g). Evidence for the morphology of the individual pear-shaped Pd islands from higher magnification AFM images is given in the Supporting Information, Fig. S2. As is found by comparing features sizes between the Au and Ag deposits (Ag structures being on average smaller than the Au structures), the average features sizes of the Pd deposits are 0.02 μm^2 (see Supporting Information, Fig. S2), smaller than those of Ag and considerably more uniformly dispersed. On Si, this is a useful finding given the catalytic poignancy of a dispersed areal population of pure Pd nanostructures.

For the Sn-containing organometallic derivative of phosphazene, pyrolysis resulted in depositions on Si and SiO_2 that are markedly different than for noble metals. As shown in Figs 1d,h, deposition on

Si results in a low roughness film containing a high density of nanoscale structures (outlined in detail further on). On SiO_2 however, thick film deposits are routinely observed, where in some instances the uniformity is interrupted by the presence of localized islands. As with all deposits in this work, previous studies[21] have conclusively shown that they are pure metals (except with Ag where some $Ag_3(PO_4)$ phase was also obtained), whereas the Sn-based surface deposit is uniquely the pyrophosphate SnP_2O_7.

We conducted careful studies of the true surface roughness of each deposit reported here and the data is shown in Fig. 2, given by

$$R_{rms} = \left[\frac{1}{N}\sum_{n=1}^{N}(y_n^2)\right]^{1/2} \quad (1)$$

where N is the number of data points of the scan profile and y_n describe the relative vertical height of the surface. Since, the surface comprises several superimposed lateral feature sizes. The measurements are bandwidth limited to a range of $L/N - L/2$, where L is the nominal AFM scan length. Typical scan lengths used here are 10 μm and the maximum lateral feature length used for the rms calculation is ~5 μm.

The rms roughness, averaged over 20 scans of different regions on each sample is plotted in Fig. 2a from which we observe a noticeable trend toward lower roughness from pyrolysis of precursors (1)-(4). The highest observed for Au structures whose deposition is always islands of varied diameter and height, to the lower roughness SnP_2O_7 deposits, which exhibit rms roughness two orders of magnitude lower in spite of their rough appearance. The effective increase in surface area was also measured and the trend, shown in Fig. 2b, follows that of the roughness parameter for the noble metals, but differs markedly for the pyrophosphate, *i.e.* the low rms roughness deposits on Si and SiO_2 of SnP_2O_7 exhibit effective surface areas greater than comparatively rougher noble metal deposits. As will be explained in more detail later, the regularity and small size of the SnP_2O_7 structures contribute to this discrepancy

where the uniform height of all features contributes to a low rms roughness, but AFM tip-radius-corrected surface areas indicate that the real exposed surface area increases by a factor of 1.07. Although an admittedly small change in effective surface area, it is still greater than the effective surface area of the Pd deposit on Si, which is composed of a high density of nanoscale metallic islands. As with all structures discussed thus far, the predominant trend is for higher roughness and effective surface area on amorphous substrates (thermally grown SiO_2).

The sensitivity of the deposited structures' roughness and surface area to the method of deposition and the substrate was also examined. By using Method B for deposition, *i.e.* by directly placing the solid precursor on Si followed by pyrolysis (skipping the solution-based evaporative step), the morphology on Si before and after inductively couple plasma (ICP) etching of the substrate surface, was examined. Using the Au-containing polymeric precursor (1) as a pertinent example of localized island growth, we find that on untreated monocrystalline Si surfaces islands of various sizes are formed, as shown in Fig. 3a (*cf.* Fig. 1a). After pyrolysis from the solid precursor, however, the film deposition is observed to comprise a morphology similar to that of electrodeposited Au (and other metals) with a grainy appearance. Atop such surfaces, we routinely observe Au rod-like features several microns in length. Based on the observations and the mechanism of pyrolysis of organometallic derivatives of phosphazene (discussed further on), the rod-like structures are elongated individual grains. AFM measurements acquired during growth show that these structures form in tandem with the main surface film, although the exact reason for their specific high-aspect ratio is as yet unclear.

Deposition on ICP etched surfaces was also examined. Among the dry etching techniques, ICP is preferable because reactive-ion etching at high-ion energies increases residual lattice damage in the semiconductor and its surface[23]. However, ICP provides the potential of achieving excellent anisotropy, low surface damage and smooth surfaces. Figures 3c,d show the morphology of the Au deposit on ICP etched Si using Methods A and B, respectively. It is immediately apparent that the shape of the Au

islands is more pronounced. In fact, this typical observation of Au on Si has been observed many times and is linked to the relationship with the Si substrate. The Au–Si system has been extensively studied and it therefore appears as a model system to address the growth of metallic nanostructures on a semiconductor surface. Several studies deal with the formation of Au islands on Si[24]. Whereas the majority of these studies focus on sub-monolayer coverage of Si with Au and subsequent island growth by the Stranski-Krastanov mechanism[25] occurring at Si(111) step edges, the knowledge is applicable to the present work since the orientation and shape of the islands formed on ICP etched Si are virtually identical. Increased order in the shape and relative position of the islands was observed after deposition by Method B without evaporation, as shown in Fig. 3d. No attempt was made here to control or prevent progressive nucleation and thus the ripeness of the island formation, rather the influence of the substrate and deposition method on as-pyrolyzed deposits is assessed. It is clear that the highest density of individual Au microstructures is obtained using solid precursors deposited on very smooth ICP etched Si, in spite of the fact that no obvious island formation (as discussed here) is observed by this route on as-received Si surfaces. The fundamental reason for this remarkable difference is related to the surface energy and is currently under study.

Mechanism of formation of the deposited structures

The mechanism of formation/deposition of the submicron structures on Si and SiO_2 surfaces by both methods is similar to the formation of other Ru, W, Fe and Si-containing nanoparticles from pyrolysis of their polyphosphazene precursors[26]. According to this mechanism, the first step involves the oxidation of the carbon atoms of the organic matter arising from the bispiro $O_2C_{12}H_8$ and from the organic groups linked to the metal atoms, *i.e.* (OC_5H_4N). This step produces a mixture of CO and CO_2 that form holes in the cyclomatrix which in turn permits the agglomeration of the metallic centers. This has been verified by TGA/DSC analysis[18]. The CO that is produced reduces the organometallic

fragment to the respective metal. The second step corresponds to the oxidation of the phosphorus atoms of the polymeric chain which produces phosphorus oxides, as well as to the elimination of fluorine and nitrogen, probably as their respective oxides. As expected, noble metals are not oxidized and remain as M^0. Simultaneously, phosphorus atoms arising from the inorganic PN backbone of the polyphosphazenes are also oxidized forming phosphorus oxides which, by reaction with the metal, form their respective metal pyrophosphates. In this step also, P_4O_7 is formed that acts as a stabilizer of the metallic nanoparticles, preventing their agglomeration.

From this mechanism, it is expected that the surface morphology and uniformity in deposition would be highly influenced by the nature of the polymer or trimeric constituent of the precursor. It is now well known that the thermal degradation of cyclotriphosphazenes often produces cyclolinear and cyclomatrix materials[27] influencing the spreading and shape of the pyrolyzed structures.

In Fig. 4, we present AFM images of the characteristic features of Ag and Pd-containing products on Si. In Fig. 4a, the typical crater formation is observed (*cf.* Fig. 1) and these appear as voids in the pure Ag film. Figure 4b shows the tear-drop Pd nanostructures. These two depositions are the morphological limits of the precursors investigated: films with voids and the opposite case of individual nanostructures on the bare substrate. For the SnP_2O_7 structures (Figs 4c,d) formed by this approach, donut shaped metal features are observed. These were also observable under SEM (Supporting Information, Fig. S3). These are similar to the tear drop Pd structures, whose morphology indicates they are donut shaped feature without center voids. Thus, once the metal centers agglomerate and pin to the surface, the resulting structure shape or morphology is thus determined by the pyrolytic combustion/decomposition mechanism of the polymer or trimer, as outlined earlier, and the agglomeration of the metal centers.

The influence of the polymeric or cyclic phosphazene precursor on the mechanism of deposit spreading was examined using AFM-based surface morphological measurements of the pyrolytic

product from (5) and (6), which are trimer-based precursors. Figure 5 shows typical AFM images of the Ag and Au surfaces from pyrolysis of their respective trimeric precursor. The as-deposited Au from trimer precursor (5) shown in Fig. 5a exhibits a more irregular deposit with localized Au island formation within a thin film (on both Si and SiO_2). This morphology is in contrast to what is found using polymeric precursors (*cf.* Fig. 1a,e and Fig. 4a above) where larger islands of greater density are formed. For the Ag deposit, a appreciable difference is observed using derivatives of phosphazenes with a trimeric constituent. Figures 5c,d show unique morphological features comprising donut-shaped Ag deposits on Si and localized smooth island deposit on SiO_2. By comparison with the deposit from polymeric precursor (*cf.* Fig. 1b,f and Scheme 2), Ag structure deposition on Si from trimeric precursors is characterized by high density island formation as opposed to cratered thin film formation; evidence for crater-like features are found in some cases (Fig. 5c). These structures (from (6)) are directly due to the cross-linking of the trimer by metal coordination, producing cyclomatrix structures as is shown in Fig. 5c.

High areal-density pyrophosphate nanostructure formation as self-affine fractal surfaces

A detailed study of the surface area coverage of the Sn-based organometallic derivative of phosphazene on Si and SiO_2 was performed to assess the prospect of creating surfaces functionalized with metal networks, useful in nanoelectronics and SERS/SEIRA for enhanced adsorbent detection sensitivity, as pertinent examples. Normally, noble metal patterned substrates are studied for SERS and SEIRA effects in addition to catalysis, as principle applications. The goal here is to compare surface deposition characteristics and to draw conclusions regarding dependence of the surface structure on the preparation procedure. The emphasis is placed on the surface coverage characteristics of the new SnP_2O_7 deposit. Although the new precursors reported here result in noble metal film and nanostructure

deposition on Si and SiO_2, their complete coverage, grainy films have been previously studied for decades.

The deposits on Si and SiO_2 are shown in the AFM images of respective surfaces, in Figs 6a-f, using Method A. Increasing the resolution of the imaging highlights the high-surface area labyrinthine nature of the SnP_2O_7 surface film. XRD studies of the deposit, shown in Fig. 6g, indicate single-crystal SnP_2O_7 formation and HRSEM investigations summarized in Fig. 6h, confirm the coral-like nature of the deposit. Details of the morphology were outlined earlier, and higher magnification AFM images show that this deposit forms as an independent film comprising a nanostructured network of SnP_2O_7 (Supporting Information, Fig. S4). Although the long-range similarity in the features is lower for the deposit on SiO_2 due possibly to the amorphous nature of the substrate, the SnP_2O_7 deposit still forms a quasi-continuous nanostructured film over areas where surface coverage is typically lowest. The detailed fundamental spreading mechanism, to be reported elsewhere, is based on the differences in Hamaker constants[28] for the metals and dielectrics and their variation as the organic matter carbonizes under thermal excitation on different substrates. This controls the formation of these structures during pyrolysis, but these measurements also show it to be sensitive to the crystallinity of the substrate. The poorest degree of coverage is always found on SiO_2 substrates, which was overcome in our experiments by varying the initial concentration of precursor on that surface.

The influence of the temperature during pyrolysis must be considered, since it is close to the oxidation temperature of Si (900 – 1200°C). The growth rate of thermal SiO_2 is typically diffusion limited and generally follows the Deal-Grove model, which is suitable for thick oxides on single crystal silicon[29]. At the pyrolysis temperature of 800°C insufficient SiO_2 formation occurs (even when pyrolysis in conducted in air and water vapor initially), to sufficiently vary the substrate morphology and significantly influence or impede the spreading of the organometallic precursor due to continued oxide thickening. In that case, Si atoms would need to diffuse through the thickening oxide and oxygen

atoms would need to diffuse through the growing SnP_2O_7 deposit, both at a temperature lower than that needed for continued diffusion-limited silicon oxidation. Thus, the differences in coverage, which are not completely understood, are related to the carbonization, polymeric dewetting and metal clustering mechanisms involved during pyrolysis primarily, with little or no oxide thickening (or influence of that thickening).

Figure 7a shows the measured surface profile for SnP_2O_7 on Si and SiO_2, averaged over 512 line profiles from several 0.5×0.5 μm^2 AFM images in contact mode. It is apparent that the deposits on both Si and SiO_2 are characterized by similar features of average widths ~25 nm. The corresponding average feature area determined from histogram profiles (Fig. 7b) of the areal variation in feature surface coverage is ~100 nm^2. Although average feature sizes are comparable, it is noted that the uppermost surface profile of the deposit on SiO_2 exhibits greater surface relief between structures than that on Si, in agreement with the overall rms roughness of similar deposits summarized in Fig. 2 and the morphology in Figs 6c and f. This difference is analogous to the resolution of the feature heights (for a given width) in Fig. 7a.

Since AFM scans are a collection of parallel line scans across two dimensions, the resulting line scans can be analyzed collectively in terms of fractional dimensionality are related back to the surface coverage characteristics. Instead of histogram and counting based methods, the nanostructured texture of the SnP_2O_7 deposit over many length scales is analyzed in the framework of a power law dependency where the fitted exponent is related to the surface fractal dimension. The variation of height fluctuations of the structures can be represented through the power spectral density (PSD) where singularities such as peaks can be used to characterise the surface, and thus the deposition, by the use of a spectrum of singularities. This allows us to treat the entire surface deposit as a self-affine fractal structure. The PSD quantity is calculated by performing a Fourier transform of the 2D height data.[30] The Fourier conjugate variable is the spatial frequency which corresponds to the lateral feature sizes,

while the strength of the distribution at each spatial frequency corresponds to average height information for those feature sizes. The PSD is given by[31]

$$PSD(f) = \frac{1}{f_s L}\left[\sum_{n=1}^{N} y_n e^{(-2\pi i f n/N)}\right]^2 \quad (2)$$

Measurements are made over a limited range and with finite resolution and the PSD is bandwidth limited with L being the total length of the scan and f the frequency from $1/L$ to $N/2L$. f_s is the sampling frequency N/L. Thus, the PSD provides information across the entire frequency range of the scanned surface from mid-frequency jaggedness to lower frequency form.

The power spectrum for real materials generally obeys a power law and can be characterized by its slope, as is the case for rough surfaces in general.[32] The PSD analysis for the SnP_2O_7 deposit is given in Figs 7c and d and described by Eq. 2. Examples of the areas examined for each substrate in this analysis are shown in Supporting Information, Fig. S5. The data show a linear behaviour on a log-log scale, characteristics of a surface exhibiting fractional dimensionality. Repeated measurements on various areas of the surface and corresponding PSD analysis gives mean power law exponents of -1.78 ± 0.13 on Si and -1.54 ± 0.17 on SiO_2. These values are clear indications of fractal dimensionality in the morphology of the deposit. Since the rms roughness is the square root of the area under the PSD curve, higher slopes in the power spectrum will result in lower rms roughness.

In AFM, analysis of the height–height correlation and the height-difference functions of surface morphologies[33] provides the lateral correlation length of the roughness as well as the roughness exponent h, which gives information on the localized 'jaggedness' of a surface for a known rms roughness[34]. For such roughness, the height–height correlation function

$$C(x) = \langle [z(x_0 + x) - \langle z \rangle][z(x_0) - \langle z \rangle] \rangle \quad (3)$$

where $z(x_0)$ is the height at a point x_0, and x is the lateral separation between two surface points, can be written in terms of σ, ξ, and h as

$$C(x) = \sigma^2 exp\,[-(|x|/\xi)^{2h}] \quad (4)$$

where σ is the rms roughness and ξ the lateral correlation length given by the value of x at which the function decays to $1/e$. This correlation function also treats the surface as self-affine fractal[35] on a short length scale, and as smooth surface on a long length scale; the data can then be compared to roughness and PSD analysis. In this approach, the amount of the diffuse component is determined by the rms roughness. The width of this component and its detailed shape give the lateral correlation length and the roughness parameter, respectively. This approach was successfully applied by Bachelet *et al.* to show how the intermediate chemically-organized surfaces occurring during progressive SrO enrichment of high-κ $SrTiO_3$ can be used as template for nanostructure fabrication of ferromagnetic oxides by chemically-driven selective nucleation[36]. In addition, recent studies by AFM of nanostructured carbon films grown by supersonic cluster beam deposition (SCBD)[37] indicate a self-affine fractal structure. This and many other approaches to fractal description of surfaces are available, but it is important to point out that most morphological measurement do not give an indication of the scale or correlation of inhomogeneities, which is very beneficial in large area deposition and self-assembly, aggregation or clustering mechanisms of materials on surfaces. The technique also aids in roughness analysis of depositions in general by considering all length scales. For the SnP_2O_7 nanostructured films reported here, we have measured a well-defined roughness exponent $h = 0.5 \pm 0.11$ (on Si) and $h = 0.75 \pm 0.13$ (on SiO_2) using AFM which was found to be independent (within the experimental error associated with multiple plots from a range of scan areas on the surface) of the average size of the features. A larger value of the roughness parameter h means more gradual height changes, which verifies the AFM line scan profiles for the respective surfaces in Fig. 7a. In these measurements self-affinity has been tested with high-aspect ratio AFM tips with nominal average radii

of 8 - 10 nm. The roughness exponent of a self-affine film should be independent of the tip radius, provided the surface correlation and scan lengths are much larger than the tip radius itself. Thus for the present work, no deconvolution of tip radius effects on measured roughness values and surface feature variations, is needed.

In addition to studies of the surface fractal dimensions, correlation studies as a function of length scale were also investigated. Length scales were varied by simply altering the scan lengths for each measurement to probe the self-similarity and long-range order in the deposits expected from power law analysis. Figure 8 shows typical AFM scans of the surface at two length scales together with corresponding self-correlation maps, for deposits on Si and SiO_2. What is observed is that the SnP_2O_7 on Si exhibits two principal spatial correlations: one with a frustrated hexagonal order for longer length scales (Fig. 8a) and the second comprising ripples in the self-correlation (Fig. 8b). The wavelength of these ripples, shown by 2D section profile extracted from the self-correlated image in Fig. 8b, is $\lambda = 326 \pm 9$ nm. It must be stated that the scan areas for these measurements were much smaller than for the computed lateral correlation lengths in Table 1 in order to achieve maximal AFM resolution. At slightly larger length scales, we observe both correlations superimposed (see Supporting Information, Fig. S6) where the ripple wavelength is $\lambda = 296 \pm 17$ nm, similar to what is measured when analyzing short length scales only, as would be expected for a self-affine fractal structure. Direct imaging of the self-affine structure by SEM gives a direct indication of the coral-like deposit. Figure 8e shows the expected self-similar morphology. At lower magnification the deposit is characterized by varying heights (brighter is higher due to dielectric charging of the surface with impinging electron flux). This is identical to the observations by AFM in Fig. 6a. At higher magnification, the features show the finer structure comprising the wavy labyrinthine arrangement of the SnP_2O_7 clusters, as was observed by AFM. At higher magnification, it is clear that the deposit is dominated by the presence of cyclic structures within the material network. This self-affine spinodal type organometallic decomposition can

be seen specifically in Fig. 8e where surrounding the white particle, which acts as a nucleation point during pyrolysis, only cyclic structures are observed. Overall the deposition is that of a self-affine arrangement of wavy and cyclic SnP_2O_7 nanostructures in a self-assembled network.

For deposits on SiO_2, the nanostructured deposit is more irregular (even from the AFM topography images) and does not show any periodic alignment at longer length scales, as judged by its diffuse self-correlated image in Fig. 8c. For short scales, some ordering is apparent and like the deposit on Si, is represented by a quasi-hexagonal form. The deposit on SiO_2 has less correlated spatial ordering compared to that on Si, but we acknowledge that the more non-uniform deposit over SiO_2 influences the correlation mapping. The stronger self-correlation of the deposit on Si is thus not believed to be linked to the surface crystallinity influence on the deposit morphology *per se* but due to the reduced coverage uniformity caused by the non-crystalline and rougher SiO_2 surface.

Thus, from the four individual metals deposited, the pyrophosphate exhibits a self-affine fractal surface comprising a labyrinthine arrangement of SnP_2O_7 on Si and SiO_2 with surface roughness and morphology amenable to several applications requiring high areal density nanostructures or deposits. Of course, significant further work outside the scope of this report is required to conclusively state the true fractal nature of the deposit through multifractal analysis and spectral analysis of the fractal exponents, but it is clear that the deposit exhibits self-affine scaling and is related to the decomposition mechanism of the precursor during pyrolysis.

As the pyrolysis was conducted in air, the presence of O_2 promotes the spreading of the product.[38] The formation of islands and craters in pyrolyzed precursor functionalized surfaces is reminiscent of the ramified-cluster-diffusion mechanism,[39] which can explain the process of spreading on the nanoscale in most studies thus far, *i.e.* bulk deposit spread in a ramified manner in the form of agglomerated cluster islands. If this and the concentration of metal centers play a significant role, as is expected based on the decomposition mechanism outlined earlier, then complete and smooth films

could be possible with further study of these precursors as well as the well defined fractal grain deposition of other metals, oxides and phosphates on Si and SiO_2.

Conclusions

We have demonstrated the fabrication of self-assembled surface deposits of micro- and nanoscale thin films and nanostructured materials of Au, Ag, Pd and Sn on silicon and silicon dioxide surfaces. The method involves the pyrolysis in air at 800°C of the respective cyclophosphazene and polyphosphazene containing the metallic derivative. To generate the depositions liquid and solid-state approaches have been used. The morphology of the as deposited structures depends on the metal used, on the nature of the surface, and on the deposition method.

Noble metals Au and Pd typically form high areal density surface deposits of metallic nanostructures, whereas Ag-based precursors form incomplete thin films. Investigation of the precursors by various methods showed the eventual deposition and nanostructure morphology to be influenced by nature of the polymer or trimeric constituent of the precursor. In addition, detailed analysis of the Sn-based deposit showed a well-defined self-affine grainy deposit on Si and SiO_2, with a characteristics labyrinthine morphology which was shown to have fractional dimensionality and long range order over many length scales. Method A affords the most uniform coverage for each type of structure, with less control over the resulting morphology coming from Method B.

The methods provide the ability to fabricate metallic micro- and nanostructures and nanostructured thin films on dielectric and semiconductor surfaces, a key technology in nanoelectronic engineering and functionalized surfaces. This solid-state method has potential applications in solid-state devices and for realizing surfaces for SERS, where a fine-tuning of the chemistry would allow rational deposition of controlled shapes and sizes of noble metal micro- and nanoparticles on technologically relevant substrates with variable smoothness, film thickness and crystal grain density.

The advantage of this appraoch over lithographic and physical deposition methods is that site specific coverage of a surface with nanostructures of a given phase in a simple and cheap manner, with clear control over the resulting phase of the deposit. Obviously, for controlled array formation, some lithographic masking must be performed. In comparison to chemical methods, most of which are restricted to Au, the advantage is the versatility. It is sufficient to choose an adequate metallic/organometallic fragment linked to the polymer/oligomer. Pyrolysis will then give the required phase.

The excellent agreement of the AFM based roughness and PSD analysis data demonstrates the advantage of understanding deposition of metal oxides and phosphates on Si and SiO_2 by AFM and associated fractal-based analysis. Since depositions of new materials requires characterization, metal clusters formed by the approach detailed here are inherently self-assembling and the fractal approach is a useful tool in comparing depositions when metal center type and concentration are varied to control morphology, for a variety of applications.

Acknowledgements

This work was supported by FONDECYT project 1085011. Part of this work was conducted under the framework of the INSPIRE programme, funded by the Irish Government's Programme for Research in Third Level Institutions, Cycle 4, National Development Plan 2007-2013. The Spanish team acknowledges the Spanish Ministerio de Educación y Ciencia (CTQ2007-67273-C02-01) and the Gobierno de Aragón for financial support. The authors also thank Prof. D. Noel Buckley for access to the Veeco Enviroscope. L. A. P. acknowledges financial support from the University of Limerick.

Supporting Information Available

Details of the synthesis of precursor (3), AFM imaging of Pd deposits and their areal density, AFM and SEM imaging of the SnP_2O_7 surface features and long-range AFM based self-correlation analysis for the Sn-based deposit. This information is available free of charge via the Internet at http://pubs.acs.org/.

References

1. Forster, S.; Antonietii, M., *Adv. Mater.* **1998,** 7, 195.
2. Love, C. J.; Estroff, L. A.; Kriebe, I. J.; Nuzzo, R. G.; Whitesides, G. M., *Chem. Rev.* **2000,** 105, 1103.
3. Tao, J.; Cheung, N. W.; Hu, C.; Kang, H. K.; Wong, S. S., *IEEE Electron Dev. Lett.* **1993,** 13, 433.
4. Cao, G., Chapter 5. In *Nanostructures and Nanomaterials*, Imperial College Press Singapore, 2004.
5. Zhu, F.; Chern, G. W.; Tchernyshyov, O.; Zhu, X. C.; Zhu, J. G.; Chien, C. L., *Phys. Rev. Lett.* **2006,** 96, 0272051.
6. Kuemmel, M.; Allouche, J.; Nicole, L.; Boissiere, C.; Laberty, C.; Amenitsch, H.; Sanchez, C.; Grosso, D., *Chem. Mater.* **2007,** 19, 3717.
7. Hong, S.; Zhu, J.; Mirkin, C. A., *Science* **1999,** 286, 523.
8. Zhang, H.; Chung, S. W.; Mirkin, C. A., *Nano Lett.* **2003,** 3, 43.
9. Haes, A.; Haynes, C. I.; McFarland, A. D.; Schartz, G. C.; Duyne, R. P. V.; Zou, S., *MRS Bull.* **2005,** 30, 368; Ding, S.; Qian, W.; Tan, Y.; Wang, Y., *Langmuir* **2006,** 22, 7105; Gao, H.; Gosvami, N. N.; Geng, J.; Tan, L.-S.; Sander, S., *Langmuir* **2006,** 22, 8078.
10. Kielbassa, S.; Kinne, M.; Behm, R. J., *Langmuir* **2004,** 20, 6644.
11. Weiss, E. A.; Kaufman, G. K.; Kriebel, J. K.; Li, Z. H.; Schalek, R.; Whitesides, G. M., *Langmuir* **2007,** 23, 9686.
12. Ahn, W.; Taylor, B.; Dall, A. G.; Roper, D. K., *Langmuir* **2008,** 24, 4174; Michalitsch, R.; Palmer, B. J.; Laibinis, P. E., *Langmuir* **2000,** 16, 6533; Takami, S.; Jenning, G. K.; Laibinis, P. E., *Langmuir* **2001,** 17, 441.
13. Wu, B.; Ho, A.; Moldovan, N.; Espinosa, H. D., *Langmuir* **2007,** 23, 9120.
14. Gudiksen, M. S.; Wang, J.; Lieber, C. M., *J. Phys. Chem. B* **2001,** 105, 4062.
15. Osawa, M.; Yoshii, K., *Appl. Spectrosc.* **1997,** 51, 512; Gay, G.; Alloschery, O.; Weiner, J.; Lezec, H. J.; O'Dwyer, C.; Sukharev, M.; Seideman, T., *Nature Phys.* **2006,** 2, 792.
16. Berry, M. V.; Hannay, J. H., *Nature* **1978,** 273, 573.
17. Barber, Z. H., *Chem. Mater.* **2006,** 16, 334; Burrel, A. K.; McCleskey, T. M.; Jia, Q. X., *Chem. Comm.* **2008,** 1271; Palgrave, P. G.; Parkin, I. P., *New J. Chem.* **2006,** 30, 505; Crozier, P. A.,

Nano Lett. **2007,** 8, 2395; Rao, C. N. R.; Muller, A.; Cheetham, A. K., *The Chemistry of Nanomaterials: Synthesis, Properties and Application*. Wiley-VCH: Verlag: Weinheim, 2004.

18. Díaz, C.; Valenzuela, M. L.; Bravo, D.; Lavayen, V.; O'Dwyer, C., *Inorg. Chem.* **2008**, 47, 11561.
19. Wu, X.; Verma, A.; Scott, K., *Fuel Cells* **2008,** 8, 453.
20. Roy, R.; Agrawal, D. K.; McKinstry, H. A., *Annu. Rev. Mater. Sci.* **1989,** 19, 59; Sleight, A. W., *Annu. Rev. Mater. Sci.* **1998,** 28, 29.
21. Jimenez, J.; Laguna, A.; Benouazzane, M.; Sanz, J. A.*;* Díaz, C.; Valenzuela, M. L.; Jones, P. G., *Chem. Eur. J*. **2009,** 15, 13509; Carriedo, G. A.; Valenzuela, M. L.; Díaz, C.; Ushak, S., *Eur. Polym. J.* **2008,** 44, 686.
22. Ferrand, P.; Egen, M.; Grieseboch, B.; Ahopelto, J.; Mueller, M.; Zentel, R.; Romanov, S. G.; Torres, C. M. S., *Appl. Phys. Lett.* **2002,** 81, 2689.
23. Lee, S.-K.; Koo, S.-M.; Zetterling, C.-M.; Östling, M., *J. Electron. Mater.* **2002,** 31, 340.
24. Swiech, W.; Bauer, E.; Mundschau, M., *Surf. Sci.* **1991,** 253, 283.
25. Homma, Y.; Finnie, P.; Ogino, T., *Appl. Phys. Lett.* **1999,** 74, 815.
26. Díaz, C.; Castillo, P.; Valenzuela, M. L., *J. Clust. Sci.* **2005,** 16, 51; Díaz, C.; Valenzuela, M. L., *J. Inorg. Organomet. Polym. Mat.* **2006,** 16, 123 ; Díaz, C.; Valenzuela, M. L., *Macromolecules* **2006,** 39, 103 ; Díaz, C.; Valenzuela, M. L.; Zúñiga, L.; O'Dwyer, C., *J. Inorg. Organomet. Polym. Mat.* **2009,** 19, 507.
27. Gleria, M.; Jaeger, R. D., *Applicative Aspects of Cyclophosphazenes* Nova Science Publishers: New York, 2004; Allcock, H. R.; McDonnell, G. S.; Riding, G. H.; Manners, I., *Chem. Mater.* **1990,** 2, 425; Brown, D. E.; Ramachandra, K.; Carter, K. R.; Allen, C. W., *Macromolecules* **2001,** 34, 2870.
28. Israelachvili, J. N., *Intermolecular and surface forces*. Academic Press: London, 1992.
29. Deal, B. E.; Grove, A. S., *J. Appl. Phys.* **1965,** 36, 3770.
30. Lita, A. E.; Jr, J. E. S., *J. Appl. Phys.* **1999,** 85, 876.
31. Elson, J. M.; Bennett, J. M., *J. Appl. Opt.* **1995,** 34, 201.
32. Angelsky, O. V.; Burkovets, D. N.; Kovalchuk, A. V.; Hanson, S. G., *Appl. Opt.* **2002,** 41, 4620.
33. Yoshinobu, T.; Iwamoto, A.; Iwasaki, H., *Jpn. J. Appl. Phys.* **1994,** 33, 383.
34. Mandelbrodt, B. B., *The Fractal Geometry of Nature*. Freeman: New York, 1982; Sinha, S. K.; Sirota, E. B.; Garoff, S.; Stanley, H. B., *Phys. Rev. B* **1988,** 38, 2297.
35. Yang, H.-N.; Wang, G.-C.; Lu, T.-M., *Diffraction from Rough Surfaces and Dynamic Growth Fronts* World Scientific: Singapore, 1993.
36. Bachelet, R.; Sánchez, F.; Santiso, J.; Munuera, C.; Ocal, C.; Fontcuberta, J., *Chem. Mater.* **2009,** 21, 2494.
37. Buzio, R.; Gnecco, E.; Boragno, C.; Valbusa, U.; Piseri, P.; Barborini, E.; Milani, P., *Surf. Sci.* **2000,** 444, L1.
38. Mestl, G.; Verbruggen, N. F. D.; Lange, F. C.; Tesche, B.; Knözinger, H., *Langmuir* **1996,** 12, 1817.
39. Song, Z.; Cai, T.; Chang, Z.; Rodriguez, G. L. A.; Hrbek, J., *J. Am. Chem. Soc.* **2003,** 125, 8059.

Figures

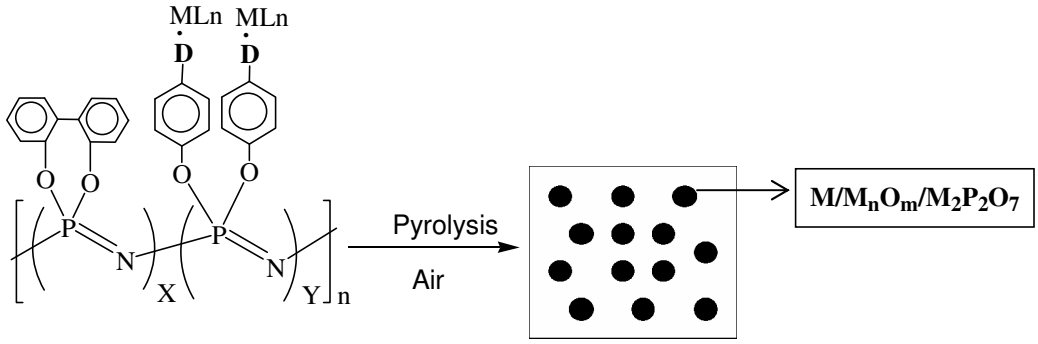

Scheme 1. Schematic representation of the preparation method of nanoparticles from polymeric metallophosphazenes, reproduced from Ref. 18.

Scheme 1

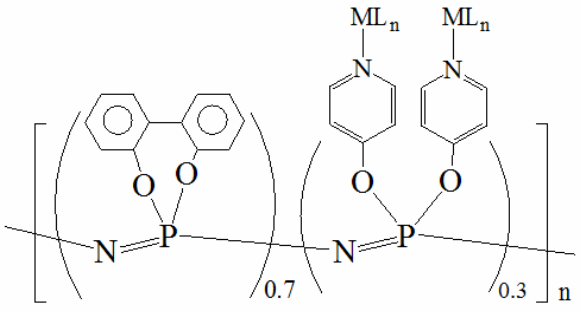

ML$_n$= AuC$_6$F$_5$ (1), Ag(OSO$_2$CF$_3$)PPh$_3$ (2), PdCl$_2$ (3)

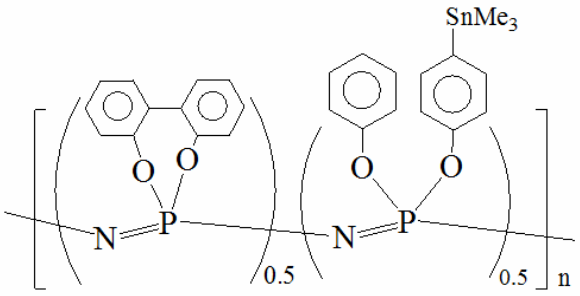

4

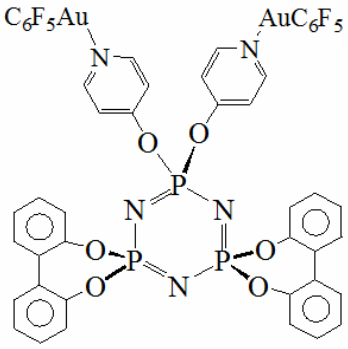

5

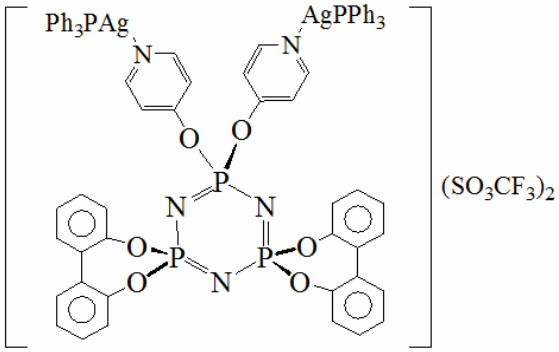

6

Scheme 2. Formulas of the phosphazenes (cyclic or polymers) used in this work as precursors.

Scheme 2

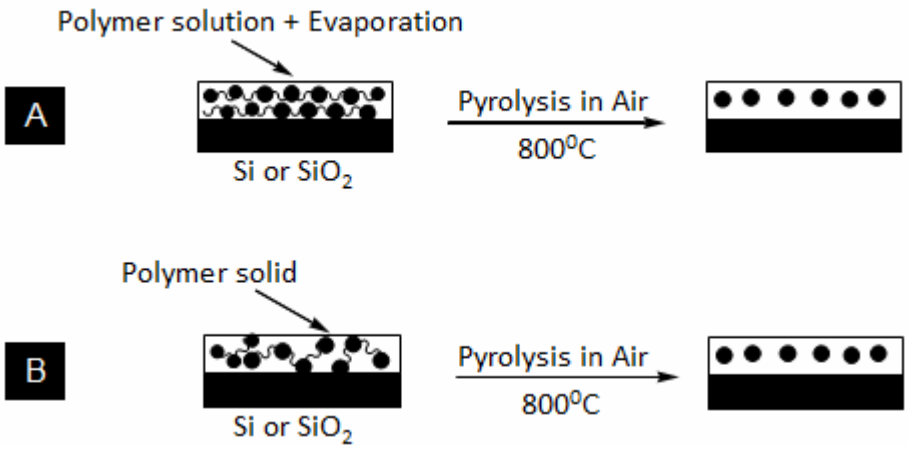

Scheme 3 Schematics of the two approaches, Method A and Method B (see main text for description) employed to created metallic nanostructured surfaces on Si or SiO_2.

Scheme 3

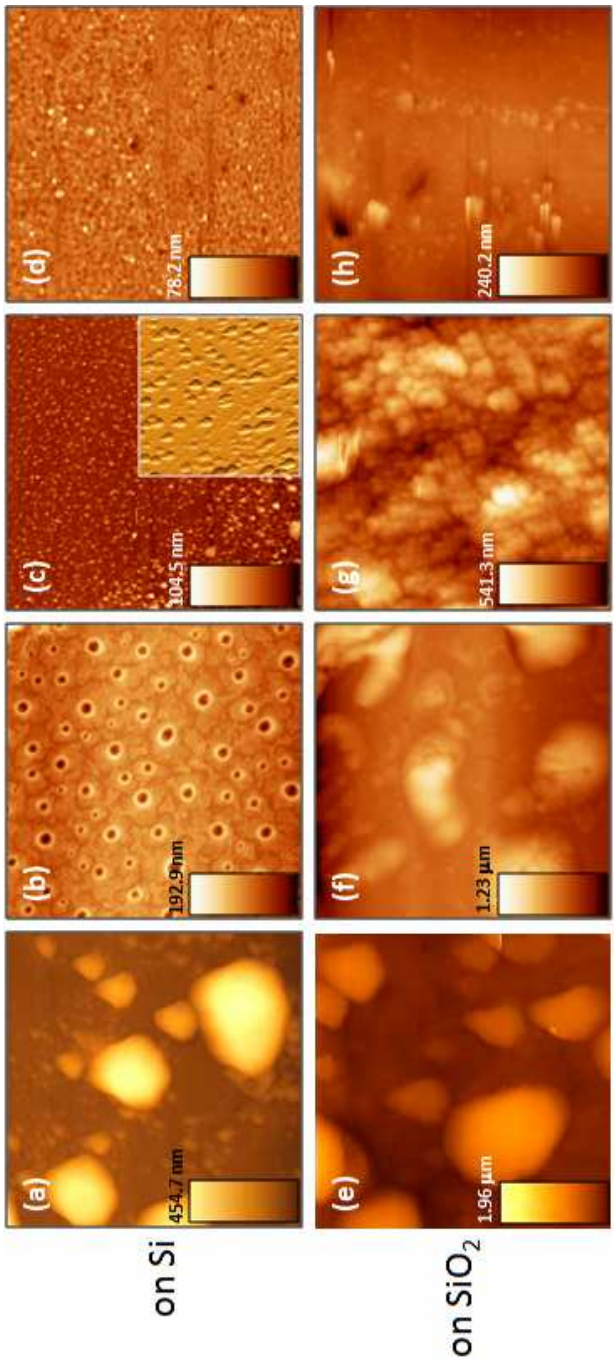

Figure 1. Contact mode AFM images of the surface morphology of metallic deposits on Si (a-d) and SiO_2 (e-h) after pyrolysis of a series of metallophosphazene precursors using Method A: (a,e) Au, (b,f) Ag, (c,g) Pd, (d,h) SnP_2O_7 (see Scheme 2 for details).

Figure 1

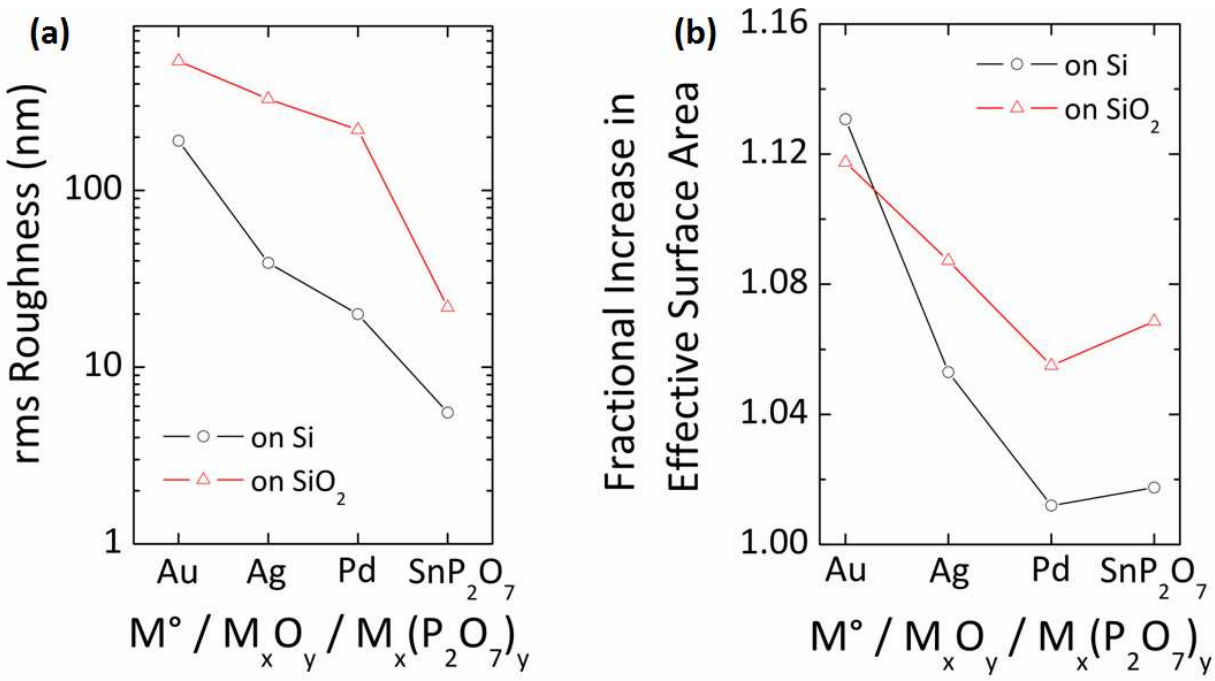

Figure 2. (a) Variation in average rms roughness derived from 15 independent scans of surfaces coated with pyrolytic products from Au, Ag, Pd, and SnP_2O_7 on Si and SiO_2. (b) Fractional increase in surface area as measured from the ratio of the total distance traveled by the tip over the 512 line scans from each image to the distance the tip would travel over the smooth nominal surface area of the Si or SiO_2 surface.

Figure 2

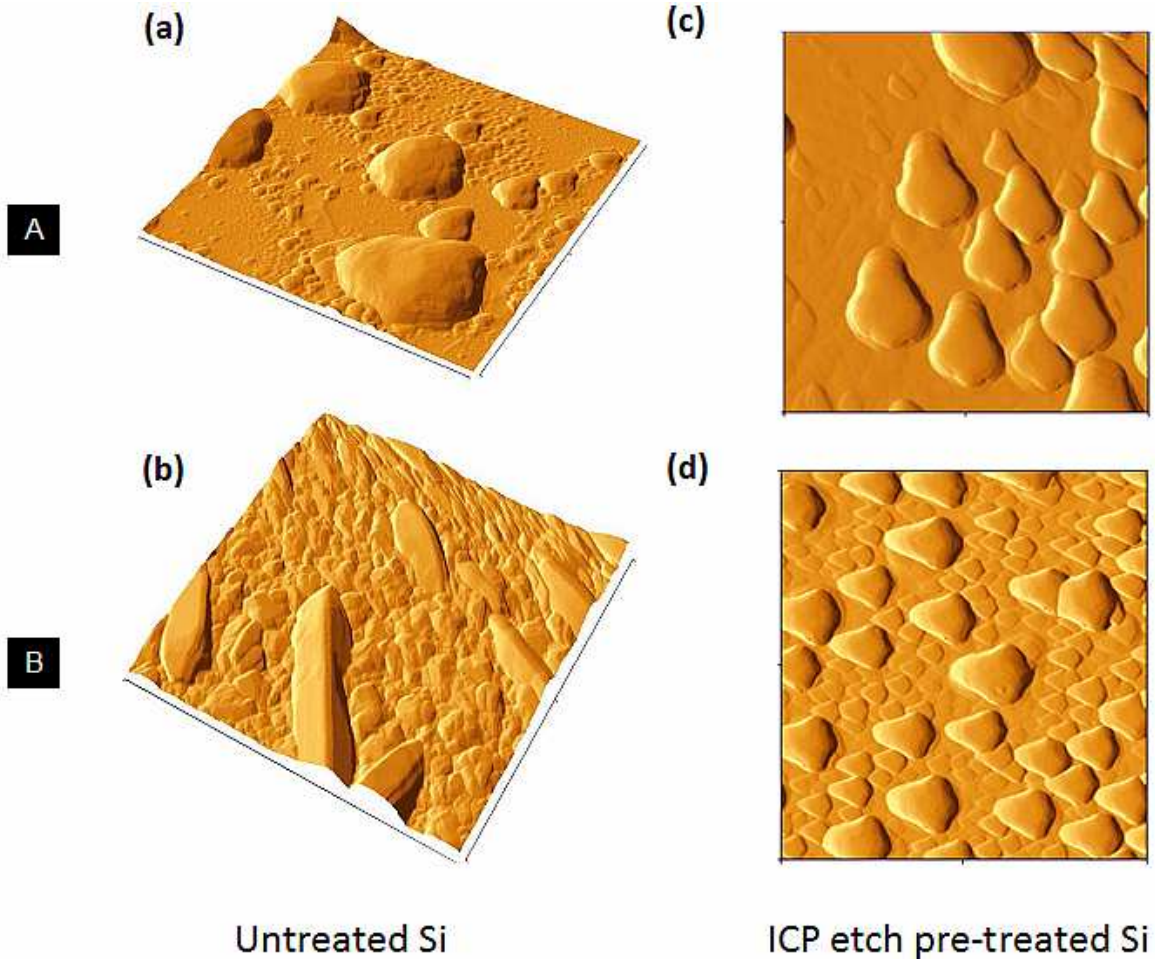

Figure 3. 10 × 10 μm^2 AFM images in contact mode of gold deposited on Si by (a) Method A and (b) Method B. Corresponding scans of pyrolytic deposition of Au-containing polymeric precursor (1) on Si after inductively coupled plasma etching. Each surface was etched to a depth of 100 nm immediately prior to placement of either liquid (Method A) or solid (Method B) deposit.

Figure 3

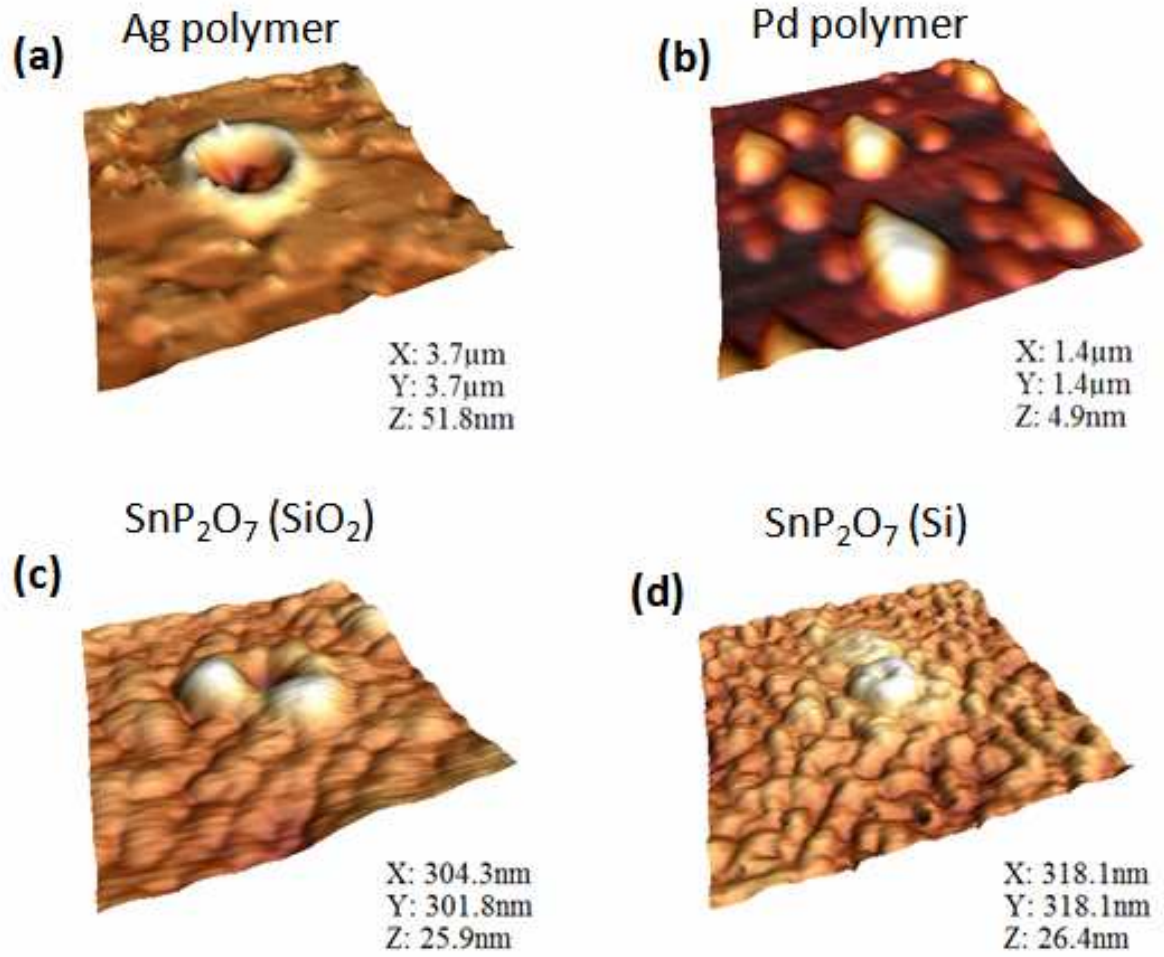

Figure 4. AFM images showing the morphology and characteristic features observed in the deposits from pyrolysis on Si of (a) the Ag polymeric precursor (2), (b) Pd from polymeric precursor (3), (c) SnP_2O_7 on SiO_2 and (d) SnP_2O_7 on Si, both from polymeric precursor (4).

Figure 4

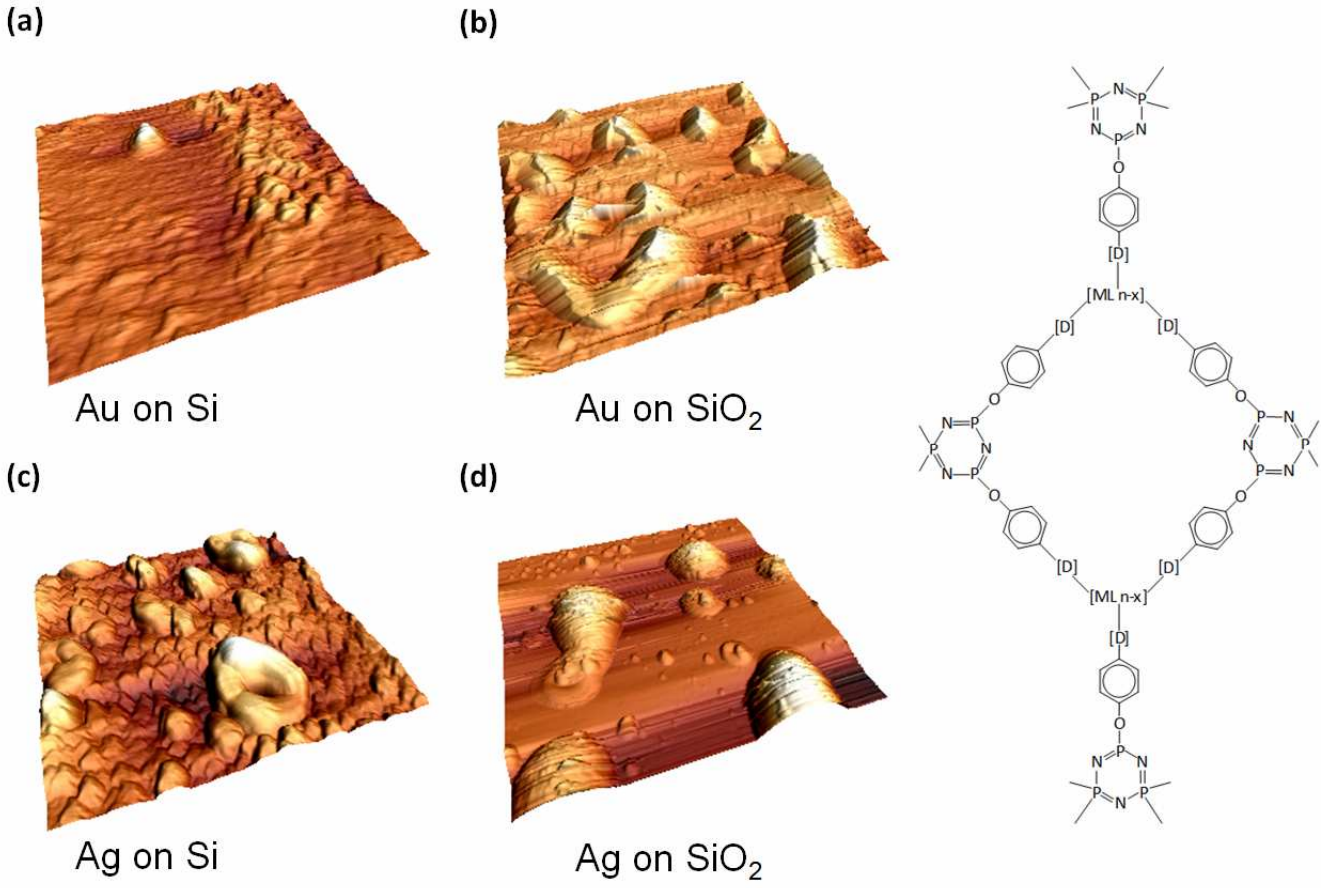

Figure 5. 5 × 5 μm^2 AFM images of the deposit morphology from pyrolysis of trimer-based organometallics containing Au on (a) Si and (b) SiO_2 and also Ag on (c) Si and (d) SiO_2. (*Right)* Schematic representation of the cyclomatrix formed during the pyrolysis of metallophosphazene derivatives of a phosphazene trimer.

Figure 5

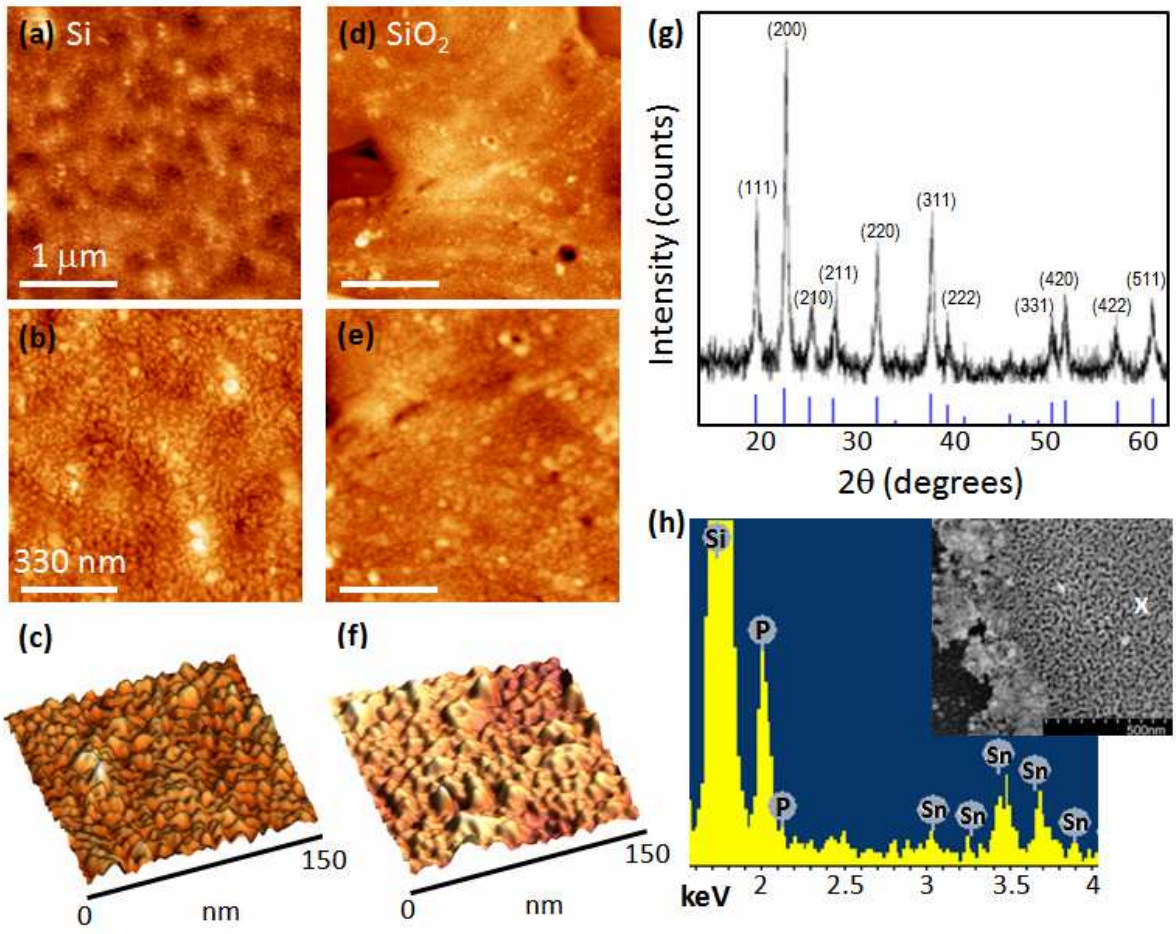

Figure 6. Morphological scans of the SnP_2O_7 product on (a-c) Si and (d-f) SiO_2 at several magnifications. The labyrinthine arrangement of the dielectric SnP_2O_7 materials is apparent, with greater surface uniformity routinely observed for deposition on Si, with a higher density of areal defects (vacancies in coverage) in depositions on SiO_2. (g) XRD pattern of the pyrolytic SnP_2O_7 product from (4) displaying only peaks corresponding to tin diphosphate, SnP_2O_7 (JCPDS card No. 00-029 1352); no peaks for SnO_2 were observed. (h) EDX spectrum acquired from localized regions of the SnP_2O_7 deposit as shown in the inset: at% Si K_α (85.32); P K_α (9.84); Sn L_α (4.84).

Figure 6

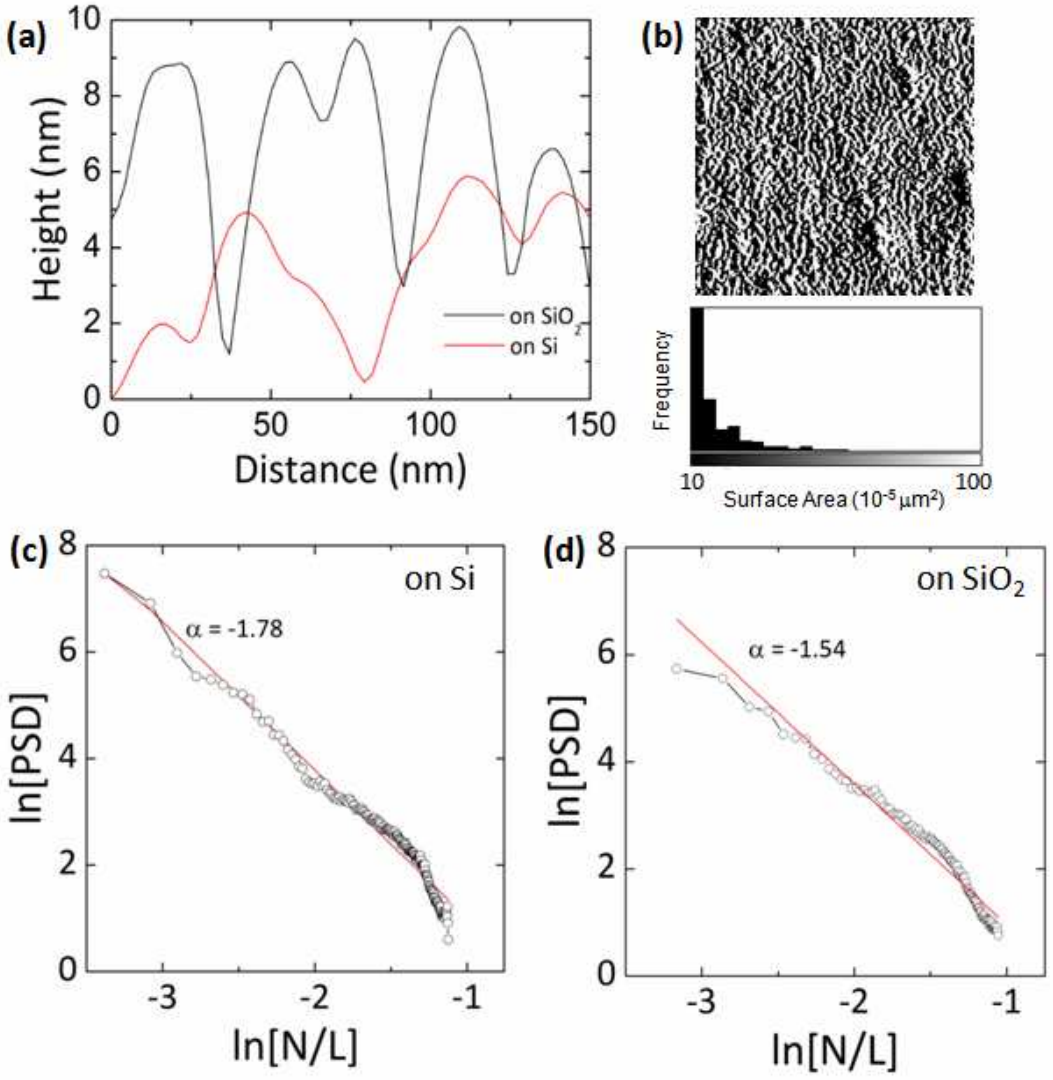

Figure 7. (a) Measured surface profile for SnP_2O_7 on Si and SiO_2, averaged over 512 line profiles from multiple 0.5 × 0.5 μm^2 AFM scans in contact mode. (b) Histogram of the average surface area of the nanostructured features from the SnP_2O_7 deposit on Si. (c) Power spectral density analysis of the self-affine fractal surface feature length scale on Si and (d) SiO_2. Only the Sn-based deposits in this work resulted in fitted exponents in the range 1.54 – 1.89 over length scales of 50 nm - 10µm. The dashed lines indicate the limits of measured slopes for different surface areas in each case.

Figure 7

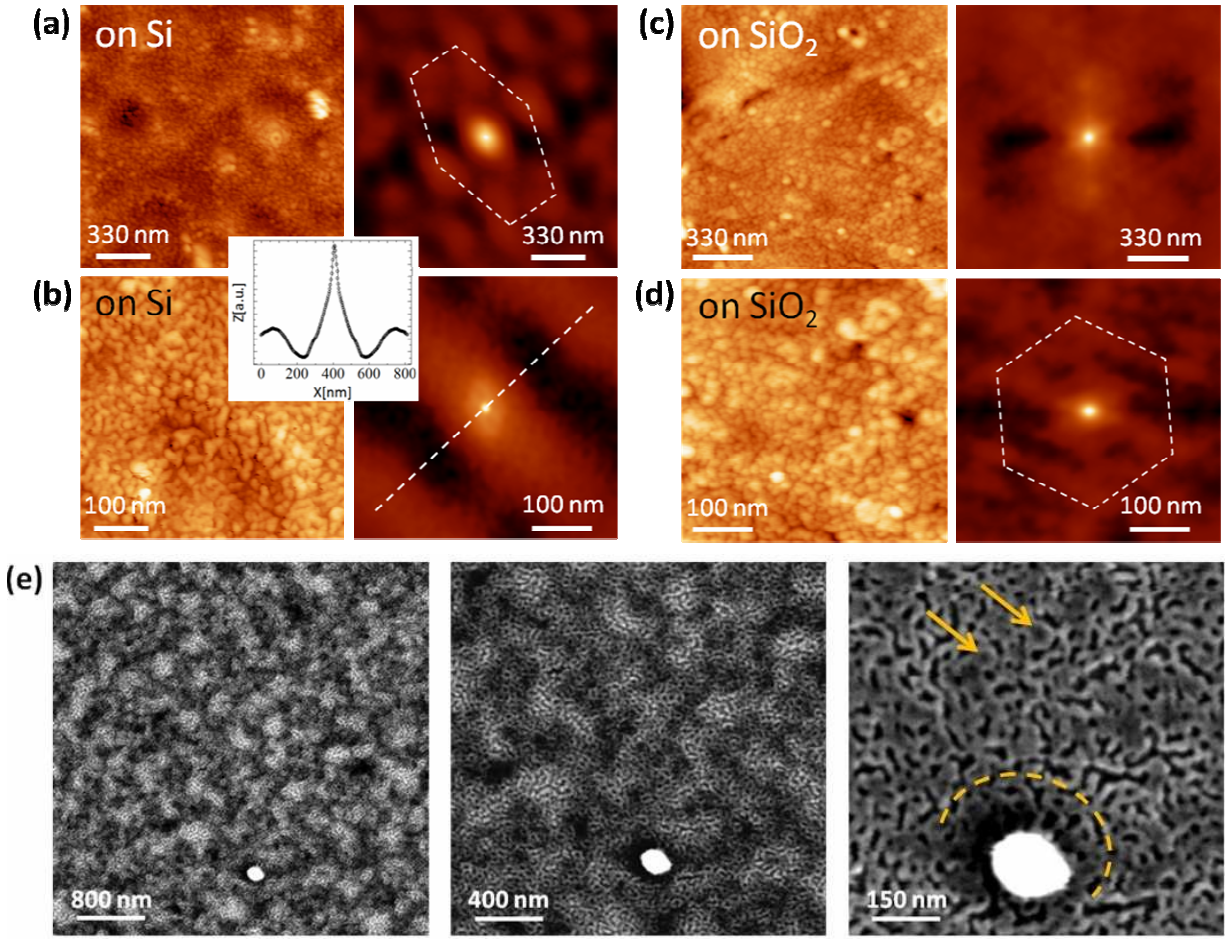

Figure 8 (a) 1.5 × 1.5 μm^2 and (b) 0.5 × 0.5 μm^2 AFM images of the SnP_2O_7 deposit on Si with corresponding correlation length maps. (*Inset*) 2D profile corresponding to the dashed line in the correlation map of AFM image (b). (c) 1.5 × 1.5 μm^2 and (d) 0.5 × 0.5 μm^2 AFM images of the SnP_2O_7 deposit on Si with corresponding correlation length maps. (e) SEM images at successively higher magnifications of a single area of deposit on Si. The white feature serves as comparison position marker and also a nucleation point for cyclic SnP_2O_7. The dashed arc delineates cyclic structures.

Figure 8